Journal of Porous Media 13(2), 125–143 (2010)

MICROSCOPIC MODELING OF THE TWO-TEMPERATURE MODEL FOR CONDUCTION IN HETEROGENEOUS MEDIA

D. A. S. Rees

[1]*Department of Mathematics, University of Bristol, Bristol BS8 1TW, UK, E-mail: ensdasr@bath.ac.uk*

[2]*Department of Mechanical Engineering, University of Bath, Bath BA2 7AY, UK (Permanent Address)*

Original Manuscript Submitted: 10/1/2007; Final Draft Received: 11/26/2008

We consider conduction in a two-phase composite solid or, equivalently, a stagnant porous medium saturated with a single fluid. In particular, we derive and calculate values for the interphase heat transfer coefficient, h, which multiplies the source/sink terms in the two-energy model for conduction in a porous medium. On allowing a uniform heat generation to take place within one of the phases, it is possible to determine h from the difference in the average temperatures of the two phases after the decay of transients. An exact analytical expression is obtained for periodic striped media, which suggests that a new nondimensional parameter might usefully be defined. Exact numerical solutions are obtained for randomly striped media. Precise expressions are also found for the two-dimensional checkerboard pattern and its three-dimensional analogue. We also consider other types of two-dimensional periodic media, and finally, randomly constituted media are analyzed.

KEY WORDS: *local thermal nonequilibrium, modelling*

1. INTRODUCTION

Situations exist where the mean local temperatures of the fluid and solid phases that comprise a porous medium have to be considered separately, rather than as a single temperature field. The use of two thermal energy equations is known variously in the published literature either as local thermal nonequilibrium (LTNE) or lack of local thermal equilibrium (LaLoThEq). When the phases are in thermal equilibrium, a single energy equation may then be used, and this situation is known as local thermal equilibrium (LTE or LoThEq). Very many papers now exist that have adopted the two–temperature model for heat transport in porous media. Applications include the drying of iron ore pellets (Ljung et al., 2008), heat exchangers (Luo et al., 2003), and geothermal energy extraction (Rees et al., 2008). In addition, very many reevaluations of classical convection problems (such as boundary layer flows and the Darcy-Bénard problem) have been undertaken; see the review by Rees and Pop (2005). There has also been a strong interest in determining conditions under which LTE may be assumed to prevail; see, for example, the papers by Lee and Vafai (1999), Khadrawi et al. (2005), and Vadasz (2005).

The first papers that used two different temperature fields are those by Anzelius (1926) and Schumann (1929), and they were both published about 80 years ago. In modern notation, their two-temperature models may be written in the form

$$\epsilon(\rho c)_{\mathrm{f}}\frac{\partial T_{\mathrm{f}}}{\partial t} = h(T_{\mathrm{s}} - T_{\mathrm{f}}) \tag{1}$$

$$(1-\epsilon)(\rho c)_{\mathrm{s}}\frac{\partial T_{\mathrm{s}}}{\partial t} = h(T_{\mathrm{f}} - T_{\mathrm{s}}) \tag{2}$$

1091-028X/10/$35.00

NOMENCLATURE

$a_{\rm sf}$	specific surface area
c	specific heat
C	constant
d	particle diameter
h	interphase heat transfer coefficient
h_R	modified interphase heat transfer coefficient
$h_{\rm sf}$	reduced form for h
H	nondimensional form of h
k	thermal conductivity
L	length scale
LTE	local thermal equilibrium
LTNE	local thermal nonequilibrium
N	number of cells in the x-direction
Pr	Prandtl number
q'''	rate of heat generation/unit volume
r	radius of circular pore
R	radius of cylinder
Re	Reynolds number
S	source term
t	time
$T_{\rm f}$	temperature of the fluid phase
$T_{\rm ref}$	reference temperature
$T_{\rm s}$	temperature of the solid phase
$\underline{v}$	velocity vector
x, y	Cartesian coordinates
Greek Symbols	
α	diffusivity ratio
$\alpha_{\rm f}$	diffusivity of the fluid phase
$\alpha_{\rm s}$	diffusivity of the solid phase
γ	porosity-scaled conductivity ratio
δ	channel width
δt	timestep
δx	spatial step
ϵ	porosity
θ	microscopic fluid temperature
Θ	macroscopic fluid temperature
λ	constant
ϕ_1, ϕ_2	functions of x
ρ	density
σ	standard deviation
Subscripts and Superscripts	
f	fluid
s	solid
p	particle/phase
u, d, r, l, c	up, down, right, left, center
$\hat{}$	modified temperature
$\bar{}$	mean value
$+, -$	opposite sides of an interface

where we see that diffusion has been neglected. In Eqs. (1) and (2), we have also neglected the advective term (viz. $u\partial T/\partial x$) that was present in the work of Anzelius (1926). The simplest equations that are now used routinely include thermal diffusion, and they take the form

$$\epsilon(\rho c)_{\rm f}\frac{\partial T_{\rm f}}{\partial t} + (\rho c)_{\rm f}\,\underline{v}.\nabla T_{\rm f} = \epsilon\nabla.(k_{\rm f}\nabla T_{\rm f}) + h(T_{\rm s} - T_{\rm f}) \tag{3}$$

$$(1-\epsilon)(\rho c)_{\rm s}\frac{\partial T_{\rm s}}{\partial t} = (1-\epsilon)\nabla.(k_{\rm s}\nabla T_{\rm s}) + h(T_{\rm f} - T_{\rm s}) \tag{4}$$

see Nield and Bejan (2006). There are more complicated models in existence that allow for cross-diffusion terms, but these are neglected in the present article. As all other quantities are easily measurable, the objective of the present study is to determine how the interphase heat transfer coefficient, h, varies as a function of the microscopic geometry of the porous medium, including its porosity and the relative conductivities and diffusivities of the phases.

Given that Eqs. (1) and (2) are linear constant-coefficient ordinary differential equations, it is straightforward to solve them analytically.

If we were to take $T \propto \exp(\lambda t)$ in Eqs. (1) and (2), then it is easy to show that

$$\lambda = 0, \quad -\Big[\frac{1}{\epsilon(\rho c)_{\rm f}} + \frac{1}{(1-\epsilon)(\rho c)_{\rm s}}\Big]\,h \tag{5}$$

The first of these values corresponds to the steady state solution of (1) and (2), with $T_{\rm f} = T_{\rm s}$ as the eigensolution corresponding to LTE. The second value of λ indicates

that, whatever the value of h, LTE is achieved relatively rapidly whenever $\epsilon \ll 1$ or $(1-\epsilon) \ll 1$, that is, when one of the phases dominates, but there is clearly a rapid evolution when h is sufficently large. It is also clear that there is a slow evolution toward thermal equilibrium when h is sufficiently small. However, it is important to note that LTE may not be attained in the presence of a fluid flow (even in the steady state; see Rees (2003) and Rees and Pop (2000)) or when one of the phases generates heat.

Attempts to determine suitable values of h have generally relied on averaging methods, and various assumptions then need to be made about closure; see the book by Whitaker (1999); the chapters by Carbonell and Whitaker (1984), Quintard et al. (1997), and Quintard and Whitaker (2000); and the paper by Quintard (1998). Hsu (1999) has also performed some closure calculations. Strictly speaking, many authors have determined expressions for $h_{\rm sf}$, rather than for h, where $h = h_{\rm sf} a_{\rm sf}$, and where $a_{\rm sf} = 6(1-\epsilon)/d_p$ has been quoted as the specific surface area of the solid phase (Dullien, 1979). These expressions include the experimental result of Wakao and Kaguei (1982),

$$h_{\rm sf} = \frac{k_{\rm f}(2 + 1.1{\rm Pr}^{1/3}{\rm Re}^{0.6})}{d_p} \tag{6}$$

the experimental result of Hwang et al. (1995),

$$h_{\rm sf} = \begin{cases} 0.004\left(\dfrac{d_\nu k_{\rm f}}{d_p^2}\right){\rm Pr}^{0.33}{\rm Re}^{1.35} & ({\rm Re} < 75) \\ 1.064\left(\dfrac{k_{\rm f}}{d_p}\right){\rm Pr}^{0.33}{\rm Re}^{0.59} & ({\rm Re} > 350) \end{cases} \tag{7}$$

where they took $a_{\rm sf} = 20.346(1-\epsilon)\epsilon^2/d_p$, and Dixon and Cresswell's (1979) formula,

$$h_{\rm sf} = \left[\frac{d_p \epsilon}{0.2555{\rm Pr}^{1/3}{\rm Re}^{2/3} k_{\rm f}} + \frac{d_p}{10 k_{\rm s}}\right]^{-1} \tag{8}$$

The numerical simulations of Kuwahara et al. (2001) of flow through a periodic array of square cylinders yielded

$$h_{\rm sf} = \frac{k_{\rm f}}{d_p}\left[\left(1 + \frac{4(1-\epsilon)}{\epsilon}\right) + \frac{1}{2}(1-\epsilon)^{1/2}{\rm Re}^{0.6}{\rm Pr}^{1/3}\right] \tag{9}$$

However, Eqs. (7) and (8) yield a zero value for h when ${\rm Re} = 0$, which implies that there is no transfer of heat between the separate phases when the porous medium is stagnant, and so the temperature fields are destined to evolve independently of one other. Equations (6) and (9) yield nonzero values for h in the absence of flow, but the resulting expressions are independent of the conductivity of the solid phase. Neither of these implications is satisfactory from a physical point of view, and it was this observation that first motivated the present work. For a stagnant porous medium, which is equivalent to a two-phase conducting composite solid, there is a degree of symmetry that must be retained in an expression for h, namely, that if one were to interchange the conductivity and volume fractions of the phases, then the expression for h should be unchanged.

The present article studies this aspect by considering various types of composite media, and it determines both analytical and numerical formulae for h which satisfy the required symmetries, although it has to be pointed out that these symmetries arise naturally from the analysis, rather than being imposed on it. This objective is achieved by means of a direct comparison between the solution of the macroscopic system given by Eqs. (3) and (4) and the solutions of detailed microscopic equations with suitable interface conditions imposed at the boundaries between the phases. We present results for both one-dimensional and two-dimensional media.

2. NONDIMENSIONALIZATION

In this analysis, we shall assume that there is no flow so that the porous medium is stagnant. The porous medium is also assumed to be periodic in structure, with the period being equal to L, which is then taken as the length scale. We shall determine h by taking a uniform rate of heat generation within the fluid phase, although the final expressions for h are independent of which phase is being heated internally. The governing macroscopic equations are

$$\epsilon(\rho c)_{\rm f}\frac{\partial T_{\rm f}}{\partial t} = \epsilon\nabla.(k_{\rm f}\nabla T_{\rm f}) + h(T_{\rm s} - T_{\rm f}) + \epsilon q_{\rm f}''' \tag{10}$$

$$(1-\epsilon)(\rho c)_{\rm s}\frac{\partial T_{\rm s}}{\partial t} = (1-\epsilon)\nabla.(k_{\rm s}\nabla T_{\rm s}) + h(T_{\rm f} - T_{\rm s}) \tag{11}$$

where all the terms in (10) and (11) have their common meanings. However, to be clear, ϵ is the porosity of the medium, and the f and s subscripts refer to the fluid and solid phases, respectively. We may nondimensionalize these equations using the following substitutions:

$$t_{\rm dim} = \frac{L^2}{\alpha_{\rm f}} t_{\rm nondim}, \quad (x,y)_{\rm dim} = L(x,y)_{\rm nondim} \tag{12}$$

$$(T_{\rm f}, T_{\rm s}) = T_{\rm ref} + \frac{q_{\rm f}''' L^2}{(\rho c)_{\rm f}\alpha_{\rm f}}(\Theta_{\rm f}, \Theta_{\rm s}) \tag{13}$$

where Θ denotes the macroscopic temperature field. Hence the macroscopic system becomes

$$\frac{\partial \Theta_{\mathrm{f}}}{\partial t} = \nabla^2 \Theta_{\mathrm{f}} + H(\Theta_{\mathrm{s}} - \Theta_{\mathrm{f}}) + 1 \tag{14}$$

$$\alpha \frac{\partial \Theta_{\mathrm{s}}}{\partial t} = \nabla^2 \Theta_{\mathrm{s}} + H\gamma(\Theta_{\mathrm{f}} - \Theta_{\mathrm{s}}) \tag{15}$$

where the quantities

$$H = \frac{hL^2}{\epsilon k_{\mathrm{f}}} \tag{16}$$

$$\gamma = \frac{\epsilon k_{\mathrm{f}}}{(1-\epsilon)k_{\mathrm{s}}} \tag{17}$$

$$\alpha = \frac{(\rho c)_{\mathrm{s}}}{(\rho c)_{\mathrm{f}}} \frac{k_{\mathrm{f}}}{k_{\mathrm{s}}} = \frac{\alpha_{\mathrm{f}}}{\alpha_{\mathrm{s}}} \tag{18}$$

are the nondimensional interphase heat transfer coefficient, the porosity-scaled conductivity ratio, and the diffusivity ratio. Of these three quantities, γ and α will be known, but H is not.

Fourier's equation applies to both phases on the microscopic level. When the same nondimensionalization is applied to the microscopic equations, then we obtain

$$\frac{\partial \theta_{\mathrm{f}}}{\partial t} = \nabla^2 \theta_{\mathrm{f}} + 1 \tag{19}$$

$$\alpha \frac{\partial \theta_{\mathrm{s}}}{\partial t} = \nabla^2 \theta_{\mathrm{s}} \tag{20}$$

where θ denotes the detailed microscopic temperature fields. These equations should be solved subject to the following continuity conditions at all interfaces:

$$\theta_{\mathrm{f}} = \theta_{\mathrm{s}} \tag{21}$$

$$k_{\mathrm{f}} \frac{\partial \theta_{\mathrm{f}}}{\partial n} = k_{\mathrm{s}} \frac{\partial \theta_{\mathrm{s}}}{\partial n} \tag{22}$$

where n denotes the direction that is normal to the interface. Solutions will also be subject to periodicity conditions at $x = 0, 1$ (and, in two dimensions, at $y = 0, 1$).

In this article, we use the lowercase notation, θ, for the detailed temperature fields on the microscopic scale, while the uppercase notation, Θ, corresponds to the temperature fields on the macroscopic scale.

The aim is to compare the solutions of the macroscopic equations, (14) and (15), with the solutions of the microscopic equations, (19) and (20), subject to the conditions (21) and (22), to find how H depends on the values of α, γ, and the porosity, ϵ. Expressions for h may then be deduced from this comparison.

For the microscopic analysis, we choose to use either a unit length in the x-direction or a unit square for the microscopic domain. These domains represent a periodic tiling in the x-direction or the x- and y-directions, respectively. Therefore the macroscopic solutions are spatially uniform and will depend only on time, and so we may neglect the diffusion terms in (14) and (15). It now becomes possible to solve the macroscopic equations analytically.

3. MACROSCOPIC SOLUTION

Given that diffusion is absent, Eqs. (14) and (15) become

$$\frac{\partial \Theta_{\mathrm{f}}}{\partial t} = H(\Theta_{\mathrm{s}} - \Theta_{\mathrm{f}}) + 1 \tag{23}$$

$$\alpha \frac{\partial \Theta_{\mathrm{s}}}{\partial t} = H\gamma(\Theta_{\mathrm{f}} - \Theta_{\mathrm{s}}) \tag{24}$$

and these are solved subject to the initial conditions, $\Theta_{\mathrm{f}} = \Theta_{\mathrm{s}} = 0$ at $t = 0$. The solution is

$$\Theta_{\mathrm{f}} = \frac{\gamma}{\gamma+\alpha}\, t + \frac{\alpha^2}{H(\gamma+\alpha)^2}\left[1 - e^{-(\alpha+\gamma)Ht/\alpha}\right] \tag{25}$$

$$\Theta_{\mathrm{s}} = \frac{\gamma}{\gamma+\alpha}\, t - \frac{\alpha\gamma}{H(\gamma+\alpha)^2}\left[1 - e^{-(\alpha+\gamma)Ht/\alpha}\right] \tag{26}$$

After transients have died out, the temperature of each phase grows at the same constant rate, with the fluid phase being the hotter as it is being heated internally. However, the difference between the temperatures tends to the constant value

$$\Theta_{\mathrm{f}} - \Theta_{\mathrm{s}} \longrightarrow \frac{\alpha}{H(\gamma+\alpha)} \quad \text{as} \quad t \longrightarrow \infty \tag{27}$$

We may now compare the detailed microscopic solutions with this formula by averaging the microscopic solutions over each phase and then finding the difference. As mentioned previously, γ and α are known, and therefore this process yields H. We shall split our analyses into two parts: one-dimensional and two-dimensional.

4. ONE-DIMENSIONAL MEDIA

4.1 Analytical Solutions for Striped Media

Consider the one-dimensional configuration shown in Fig. 1, a periodic striped domain, where the fluid phase corresponds to the black region and the solid phase to the white region, and where the porosity is ϵ. Equations (19) and (20) apply in $x < \pm\epsilon/2$ and $\epsilon/2 \le |x| \le 1/2$, respectively, while the interface conditions (21) and (22)

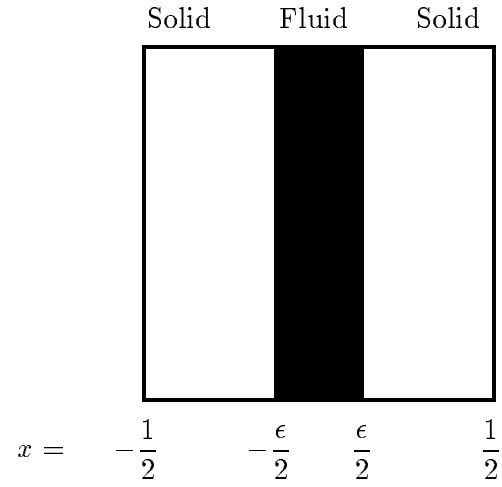

FIG. 1: Showing one period of a one-dimensional striped medium with porosity ϵ

are applied at $x = \pm\epsilon/2$ and periodicity is imposed at $x = \pm 1/2$. On ignoring decaying transients, we find that the linearly growing solution takes the form

$$\theta_f = t\,\phi_{1f}(x) + \phi_{2f}(x), \quad \theta_s = t\,\phi_{1s}(x) + \phi_{2s}(x) \tag{28}$$

for each phase. We find that

$$\phi_{1\mathrm{f}} = \phi_{1\mathrm{s}} = C_1 \tag{29}$$

while

$$\phi_{2\mathrm{f}} = \left(\frac{C_1 - 1}{2}\right) x^2 + C_2 x + C_3 \tag{30}$$

$$\phi_{2\mathrm{s}} = \frac{\alpha C_1}{2}\left(|x| - \frac{1}{2}\right)^2 + C_3 \tag{31}$$

The constants C_1 and C_2 are easily shown to be

$$C_1 = \frac{\epsilon k_\mathrm{f}}{\epsilon k_\mathrm{f} + \alpha(1-\epsilon)k_\mathrm{s}} = \frac{\gamma}{\gamma + \alpha} \tag{32}$$

$$C_2 = \frac{1}{8}\epsilon(1-\epsilon)\left[\frac{\epsilon}{k_\mathrm{f}} + \frac{1-\epsilon}{k_\mathrm{s}}\right] k_\mathrm{f} \tag{33}$$

and C_3 is arbitrary (or rather, it depends on any initial conditions that are imposed in an unsteady simulation). It is important to note that the value of the coefficient C_1 given in Eq. (32) is precisely the growth rate of the temperature rise in both phases (see Eqs. (28) and (29)), and this matches exactly with the macroscopic analysis (see Eqs. (25) and (26)).

For comparison with the macroscopic solution, we need to find the intrinsic temperature of each phase by averaging the two temperatures over their respective regions:

$$\bar{\phi}_{2\mathrm{f}} = \frac{2}{\epsilon}\int_0^{\epsilon/2} \phi_{2\mathrm{f}}\,dx \tag{34}$$

$$\bar{\phi}_{2\mathrm{s}} = \frac{2}{(1-\epsilon)}\int_{\epsilon/2}^{1/2} \phi_{2\mathrm{s}}\,dx \tag{35}$$

and to find the difference:

$$\bar{\phi}_{2\mathrm{f}} - \bar{\phi}_{2\mathrm{s}} = \frac{1}{12}\frac{\alpha}{\gamma+\alpha}\epsilon k_\mathrm{f}\left[\frac{\epsilon}{k_\mathrm{f}} + \frac{1-\epsilon}{k_\mathrm{s}}\right] \tag{36}$$

This may be equated with the value given in (27), and hence

$$H = \frac{12}{\epsilon k_\mathrm{f}\left[\dfrac{\epsilon}{k_\mathrm{f}} + \dfrac{1-\epsilon}{k_\mathrm{s}}\right]} \tag{37}$$

The corresponding value of h, obtained from (16), is

$$h = \frac{12}{L^2\left[\dfrac{\epsilon}{k_\mathrm{f}} + \dfrac{1-\epsilon}{k_\mathrm{s}}\right]} \tag{38}$$

For this very simple configuration, we have obtained an analytical form for h, and it does indeed satisfy the appropriate symmetry: if the conductivities and the volume fractions of the phases are swapped, then the expression remains the same.

This analysis illustrates our general approach to finding h: we first calculate H using

$$\frac{\alpha}{H(\gamma+\alpha)} = \bar{\phi}_{2\mathrm{f}} - \bar{\phi}_{2\mathrm{s}} \tag{39}$$

where $\bar{\phi}_{2\mathrm{f}} - \bar{\phi}_{2\mathrm{s}}$ is found either analytically or numerically, then h is obtained using (16), and finally, we determine the value of the quantity

$$h_{_R} = hL^2\left[\frac{\epsilon}{k_\mathrm{f}} + \frac{1-\epsilon}{k_\mathrm{s}}\right] \tag{40}$$

The present striped medium is therefore characterized by having the constant value $h_{_R} = 12$. This value is independent of the porosity, conductivities, and diffusivities of the porous medium.

4.2 Solutions for Random Media

In this subsection, we shall replace the configuration shown in Fig. 1 with one where there are N vertical strips of uniform width, where the assignment of a phase to each strip is random. Therefore we consider a one-dimensional periodic medium where the composition of the repeating unit is random; see Fig. 2 for a typical example.

The solution procedure for this more general problem is facilitated by first subtracting out the linearly growing component of the solution,

$$\theta_{\mathrm{f,s}} = \frac{\gamma}{\gamma+\alpha}t + \hat{\theta}_{\mathrm{f,s}} \tag{41}$$

to obtain the equations

$$\frac{d^2\hat{\theta}_{\mathrm{f}}}{dx^2} = -\frac{\alpha}{\gamma+\alpha}, \qquad \frac{d^2\hat{\theta}_{\mathrm{s}}}{dx^2} = \frac{\alpha\gamma}{\gamma+\alpha} \tag{42}$$

and these are also subject to the interface conditions (21) and (22) and suitable periodicity conditions. The manner in which solutions for N strips may be obtained follows roughly the methodology used in Section 4.1, but as it is quite lengthy to present, we omit it for the sake of brevity. However, it is a straightforward direct method with an operation count that is proportional to N and is simple to encode. Once a solution is found for a given set of N strips, the mean temperatures of each phase are found.

Given that the number of strips is N, the total number of possible two-phase configurations that exist is $2^N - 2$; the two that are missing correspond to a pure fluid and to a pure solid. We note that all those configurations that are equivalent to any chosen one by virtue of translation and/or reflection (such as SSSSFFSF, FSSSSFFS, and FFSSSSFS) are all counted within this total, that is, all possible combinations of phases are taken. When $N \leq 30$, we are able to determine $h_{_R}$ for every single possible configuration; for $N = 30$, this is a set of $1,073,741,822$ different cases whose computation took roughly 80 minutes, and therefore it is possible to analyze these cases in as much detail as is needed. In particular, for each possible porosity (viz. multiples of $1/N$), we have determined both the mean value of $h_{_R}$ (denoted as $\bar{h}_{_R}$) and its standard deviation, $\sigma(h_{_R})$. However, when $N > 30$, the number of combinations becomes too great to compute, and therefore we have approximated the required statistics using 10^5 random configurations for each porosity. In general, we find that this number is sufficient to give accuracy to roughly three or four significant figures. Therefore we were able to consider cases where N is as large as 1000.

As in Section 4.1, we find that $h_{_R}$ is independent of the conductivities and diffusivities of the phases, which simplifies the presentation of our results. As we shall see later, there are configurations in which $h_{_R}$ does depend on the conductivity ratio, but there is indeed a general result that applies to all configurations in one, two, and three dimensions. We note first that both the right-hand-side terms in (42) are proportional to $\alpha/(\gamma+\alpha)$. Second, the interface and periodicity conditions are homogeneous. Therefore we may deduce that both $\hat{\theta}_{\mathrm{f}}$ and $\hat{\theta}_{\mathrm{s}}$ are proportional to $\alpha/(\gamma+\alpha)$, and so Eq. (39) leads to the fact that H (and hence $h_{_R}$) is independent of $\alpha/(\gamma+\alpha)$. Given that solutions do generally depend on γ, it is clear that $h_{_R}$ must be independent of α. This argument also applies in two and three dimensions where the second derivatives in (42) are replaced by Laplacians. This general result was also confirmed numerically.

Figure 3 shows all the possible $h_{_R}$ values lying below 250 that may be obtained for $N = 10$ and $N = 15$. Also shown are both the mean value, $\bar{h}_{_R}$, and one standard deviation from the mean ($\bar{h}_{_R} \pm \sigma(h_{_R})$) for $N = 10$, 15, 20, and 30. We note that both the exact analysis and the 10^5 random cases are drawn for $N = 20$ and 30, and the differences are negligible.

In all these cases, and indeed, for all values of N, the smallest value that may be taken by $h_{_R}$ is 12, and this corresponds to those cases where the fluid phase strips are all grouped together. In other words, this situation corresponds precisely to that described in Section 4.1. On the other hand, whenever N is even, the largest possible value for $h_{_R}$ is $3N^2$ when $\epsilon = 0.5$. This configuration corresponds to alternating phases, and therefore N strips corresponds to $N/2$ pairs, for which the appropri-

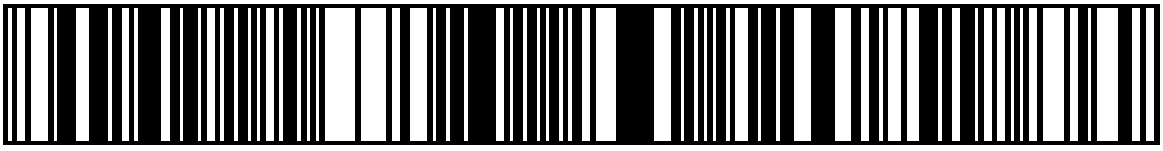

FIG. 2: Showing one period of a one-dimensional, randomly striped medium with porosity 0.5 and $N = 256$ strips

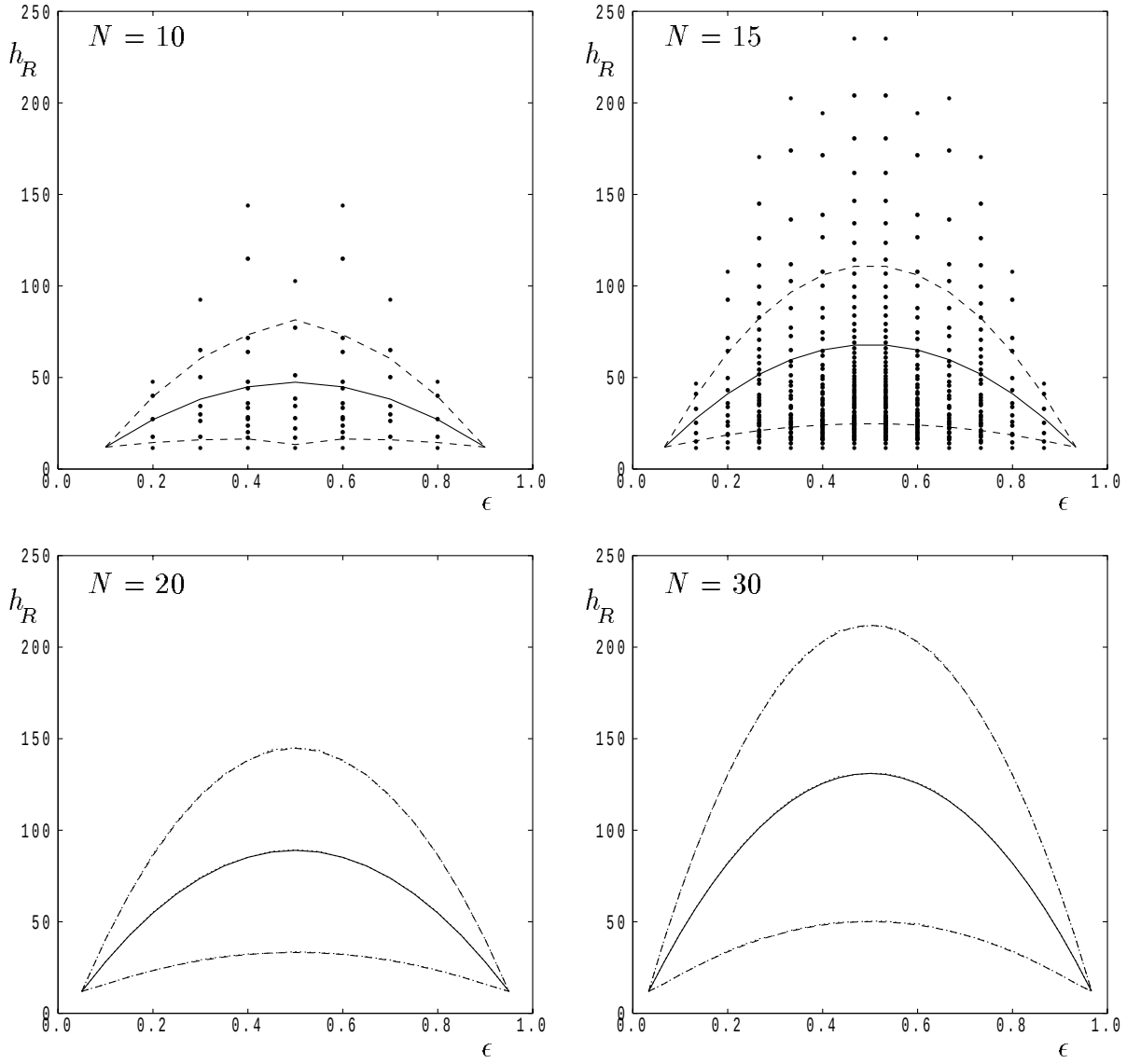

FIG. 3: Showing h_R–values (bullets) for $N = 10$ and $N = 15$, and the variation of $\bar{h}_R$ (solid lines) and one standard deviation from the mean (dashed lines) for $N = 10$, 15, 20, and 30. Also shown are the curves corresponding to 10^5 random cases (dotted lines).

ate length scale for the purposes of nondimensionalization should have been $2L/N$, rather than L. Therefore the heat transfer coefficient from the "point of view" of the present nondimensionalization is $h_R = 12/[2/N]^2 = 3N^2$.

Generally, the larger the number of interfaces between the phases, the larger is the value of h_R. However, the value of h_R is very highly sensitive to the number of interfaces when the number of interfaces is large. For example, when $N = 10$, the configuration SFSFSFSFSFSF has $h_R = 300$, but this is reduced to $h_R = 102.7397$ on swapping the members of any neighboring pair, such as SFFSSFSFSF. Thus the values of h_R tend to be concentrated much closer to 12 than to $3N^2$ for general values of N, as seen in the upper frames of Fig. 3.

For all values of N, the shape of the $\bar{h}_R$ curve is roughly parabolic, as are the curves for $\bar{h}_R \pm \sigma(h_R)$. In

all cases one standard deviation is quite large compared with the magnitude of $\bar{h}_R$ itself. In addition, the maximum value of h_R, which occurs at $\epsilon = 0.5$ when N is even, also grows with N. The large-N behavior of these has been considered; the variation of both $\bar{h}_R$ and $\sigma(h_R)$ are tabulated in Table 1 for increasing values of N up to $10,000$, and for both $\epsilon = 0.5$ and $\epsilon = 0.2$. It seems clear, from Table 1, that the ratio of $\sigma(h_R)$ and $\bar{h}_R$ is roughly constant, and approximately equal to 0.6. This is not only true for both the porosities chosen for inclusion in the table, but also for other porosities that are not close to $1/N$ or $1 - 1/N$ (for which $\bar{h}_R$ is close to 12 and $\sigma(h_R)$ is close to zero). Thus the shape of the curve is essentially independent of N when N is large.

A quick glance at the values of $\bar{h}_R$ and $\sigma(h_R)$ given in Table 1 suggests that they are both proportional to N. This is confirmed in Table 1, which tabulates values of $\bar{h}_R/N$. The numerical data for these and other values of ϵ (not shown here) also suggest that the variation of $\bar{h}_R/N$ with ϵ approximates a parabolic function very well indeed. On taking the maximum value of $\bar{h}_R/N$ to be roughly 4.2 when $\epsilon = 0.5$, it is straightforward to obtain the correlation

$$\bar{h}_R \sim 4.2N \times 4\epsilon(1-\epsilon) \tag{43}$$

and therefore we may obtain the formula,

$$\bar{h} \sim \frac{16.8N\epsilon(1-\epsilon)}{L^2\left[\frac{\epsilon}{k_\mathrm{f}} + \frac{1-\epsilon}{k_\mathrm{s}}\right]} \tag{44}$$

for the mean value of h where the standard deviation is roughly 0.6 of this value. We note that this formula is very accurate when N is sufficiently large (where the results shown in Table 1 suggest that $N \geq 100$ is a good lower bound) and when neither ϵ nor $1 - \epsilon$ is close to $1/N$.

5. TWO-DIMENSIONAL MEDIA

5.1 Numerical Method

We now deal with the solution of the microscopic equations in two-dimensional domains by using finite differences. We consider a square region divided into an $N \times N$ array of subsquares, each of which corresponds to one of the two phases, and therefore each has its own rate of heat generation (either 1 or 0), its own thermal conductivity (k_f or k_s), and its own thermal diffusivity (α_f or α_s.) Given the length of time that is required to solve the one-dimensional problem whenever $N > 30$, it is clear that comprehensive and accurate solutions in two dimensions cannot be obtained easily unless N is less than or equal to 5, or possibly 6. Therefore we have to adopt the strategy of running a fixed number of random cases for all values of N.

We used two different methods of solution: (1) a simple Euler method for timestepping and (2) a method that determines only the steady part of the evolving solution. Method (1) was used for the checkerboard and box domains that are described later, but method (2) was found to yield solutions more quickly for the randomly assigned domains.

The governing microscopic equations may be written in the form

$$\alpha_p \frac{\partial \theta}{\partial t} = \nabla^2 \theta + S_p \tag{45}$$

TABLE 1: Values of $\bar{h}_R$, $\sigma(h_R)$ and their ratio for increasing values of N, $\epsilon = 0.5$, and $\epsilon = 0.2$

	$\epsilon = 0.5$				$\epsilon = 0.2$			
N	$\bar{h}_R$	$\sigma(h_R)$	$\bar{h}_R/\sigma(h_R)$	$\bar{h}_R/N$	$\bar{h}_R$	$\sigma(h_R)$	$\bar{h}_R/\sigma(h_R)$	$\bar{h}_R/N$
30	131.07	80.78	0.616	4.369	82.25	48.28	0.586	2.745
100	426.40	258.16	0.605	4.264	272.04	163.08	0.599	2.720
200	848.34	513.28	0.605	4.242	542.22	324.57	0.599	2.711
500	2110.55	1263.55	0.599	4.221	1350.72	811.07	0.600	2.701
1000	4213.93	2527.97	0.600	4.214	2691.72	1615.81	0.600	2.692
2000	8542.79	5101.51	0.597	4.227	5389.08	3219.30	0.597	2.694
5000	21132.85	12647.55	0.598	4.227	13484.32	8097.97	0.600	2.697
10000	42544.11	25304.30	0.595	4.254	27082.48	16184.22	0.598	2.708

subject to the interface conditions,

$$\theta^- = \theta^+, \quad k^- \frac{\partial \theta^-}{\partial n} = k^+ \frac{\partial \theta^+}{\partial n} \tag{46}$$

where *(i)* n denotes the normal derivative, the phase, *(ii)* p, may be either fluid or solid, and *(iii)* the symbols $-$ and $+$ correspond to the limiting values from each side of an interface. Finite difference nodes were placed at the corners of the subsquares, as shown in Fig. 4, where i and j denote grid points in the x- and y-directions, respectively. We take second order central differences at each (i, j) location. For each node, these are taken from 'the point of view' of each of the four neighboring regions. This introduces eight fictitious points. There are also four interface conditions for the heat flux, each of which may be applied from the point of view of each side of the interface, thereby using the same eight fictitious points. It turns out that the four different finite difference approximations may be added together and the eight fictitious points eliminated using the interface conditions. As a result of this process, we obtain the finite difference approximation

$$\begin{aligned}
&\left(k^{++}\alpha^{++}+k^{+-}\alpha^{+-}+k^{-+}\alpha^{-+}+k^{--}\alpha^{--}\right)\\
&\times \theta_{i,j}^{n+1} = \left(k^{++}\alpha^{++}+k^{+-}\alpha^{+-}+k^{-+}\alpha^{-+}\right.\\
&\left.+k^{--}\alpha^{--}\right)\theta_{i,j}^{n} + \frac{\delta t}{\delta x^2}\begin{pmatrix} 0 & C_u & 0 \\ C_l & -C_c & C_r \\ 0 & C_d & 0 \end{pmatrix}\theta_{i,j}^{n}\\
&+ \delta t\left(k^{++}S^{++}+k^{+-}S^{+-}+k^{-+}S^{-+}\right.\\
&\left.+k^{--}S^{--}\right)
\end{aligned} \tag{47}$$

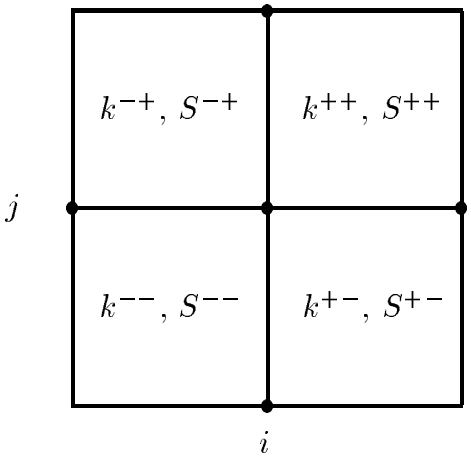

FIG. 4: Depicting a random set of four subsquares and the notation used for the finite difference approximation

where δt is the timestep, δx is the spatial step in both the x- and y-directions, and the constants in the finite difference molecule are

$$\begin{aligned}
C_c &= 4(k^{++} + k^{+-} + k^{-+} + k^{--})\\
C_r &= 2(k^{++} + k^{+-})\\
C_l &= 2(k^{-+} + k^{--})\\
C_u &= 2(k^{++} + k^{-+})\\
C_d &= 2(k^{+-} + k^{--})
\end{aligned} \tag{48}$$

This timestepping method works well for structured media in which large clusters of single-phase material exist, but transients die out slowly for random media. Therefore, for random media, the method was modified by again subtracting out the linearly growing part of the solution to obtain a pair of Poisson equations for the remaining steady part of the solution. Therefore we made the substitutions

$$\theta_{\mathrm{f,s}} = \frac{\gamma}{\gamma + \alpha} t + \hat{\theta}_{\mathrm{f,s}} \tag{49}$$

The equations for $\hat{\theta}_{\mathrm{f}}$ and $\hat{\theta}_{\mathrm{s}}$ are now

$$\nabla^2 \hat{\theta}_{\mathrm{f}} + \frac{\alpha}{\gamma + \alpha} = 0, \qquad \nabla^2 \hat{\theta}_{\mathrm{s}} - \frac{\alpha\gamma}{\gamma + \alpha} = 0 \tag{50}$$

and these are subject to the same interface and periodicity conditions. Equations (50) were solved using a pointwise multigrid method. Solutions were checked against those obtained using the unsteady method described earlier and were found to be identical to within convergence tolerances.

We attempted to employ the compact finite differences methodology to these equations to obtain fourth-order accurate solutions, but too few equations were obtained to eliminate the extra number of fictitious points that were generated.

5.2 Checkerboard Patterns

The checkerboard pattern simply consists of alternating squares of fluid and solid, as indicated in Fig. 5.

Numerical simulations were run for the following number of gridpoints in each direction, $N = 10$, 20, 40 and 80, and for a variety of values of the conductivities, and the diffusivities. It was found once more that the value for h_R is a constant, that is, it is independent of both the conductivity ratio, $k_{\mathrm{s}}/k_{\mathrm{f}}$, and the diffusivity ratio, α.

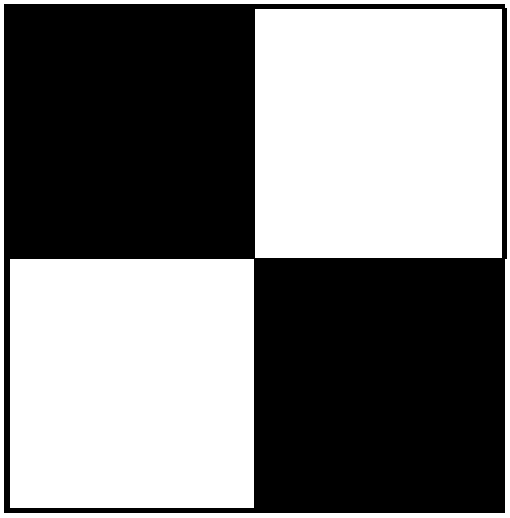

FIG. 5: Depicting a checkerboard pattern of fluid (black) and solid (white)

As the spatial discretization is of second-order accuracy, the raw data obtained were improved by the application of Richardson's extrapolation, and the extrapolates, now of fourth-order accuracy, were themselves extrapolated once more. Our computations are summarized in Table 2.

Therefore we may state that

$$h = \frac{28.4542}{L^2\left[\dfrac{\epsilon}{k_{\rm f}} + \dfrac{1-\epsilon}{k_{\rm s}}\right]} = \frac{56.9084}{L^2\left[k_{\rm f}^{-1} + k_{\rm s}^{-1}\right]} \qquad (51)$$

for two-dimensional checkerboard patterns, since $\epsilon = 0.5$. It is of interest to note that the reciprocal of 28.4542 is 0.035144, which is precisely the value obtained by solving the two-dimensional Poisson's equation, $\nabla^2\psi = -1$, on the unit square with the boundary conditions, $\psi = 0$, on all four boundaries, and then integrating that solution for ψ over the unit square. That this should be so may be understood by first appealing to the symmetries of the checkerboard pattern. The numerical solution for this pattern consists precisely of the same solutions of Poisson's equation within each subsquare (albeit in regions of side 0.5), where the amplitude of the solutions in neighboring regions are in the precise ratio, $-\gamma$. Given that $\epsilon = 0.5$, γ is exactly the conductivity ratio, and therefore the correct interface conditions are satisfied by such a patchwork of individual solutions of Poisson's equation. The averaging process required to find the intrinsic temperatures of each phase is then analogous to the integral of ψ. As a consequence of this, the temperature is also uniform along the interfaces.

TABLE 2: Giving values of $h_{_R}$ and successive Richardson extrapolates as a function of the number of gridpoints, N

N	$h_{_R}$	R.E.	R.E.^{2}
10	32.32759		
20	29.38612	28.40563	
40	28.68561	28.45211	
80	28.51197	28.45409	28.45422

The analogous three-dimensional configuration consisting of alternating cubes was considered by employing a simple extension to the numerical scheme. We omit the details, which are straightforward, but we find that

$$h = \frac{49.5833}{L^2\left[\dfrac{\epsilon}{k_{\rm f}} + \dfrac{1-\epsilon}{k_{\rm s}}\right]} = \frac{90.1666}{L^2\left[k_{\rm f}^{-1} + k_{\rm s}^{-1}\right]} \qquad (52)$$

for three-dimensional checkerboards. Again, these numerical values bear the same relation to the integral of the solution of a three-dimensional Poisson's equation, as detailed earlier.

5.3 Box Configurations

We now consider box patterns, as illustrated in Fig. 6. These arise in two types, namely, those for which the heat-generating phase is either percolating or nonpercolating, where it is important to recall that the square domains shown in Fig. 6 form the repeating units in a periodic porous medium.

Computations were undertaken on an 80×80 grid of subsquares, with the central heat-generating square forming an $n \times n$ set of subsquares with $n = 10, 20, \cdots, 70$. Therefore the porosity is $\epsilon = n^2/N^2$. Solutions were obtained for a wide range of conductivity ratios, and the variation of $h_{_R}$ with conductivity ratio for the chosen values of n are shown in Fig. 7. It is clear from this figure that there is a variation in the value of $h_{_R}$ with conductivity ratio, but that constant values are obtained in both the small and large limits of the conductivity ratio.

When $k_{\rm s} \gg k_{\rm f}$, a detailed examination of the numerical values for $h_{_R}$ shows clearly that $h_{_R}/n^2 \simeq 0.00445$.

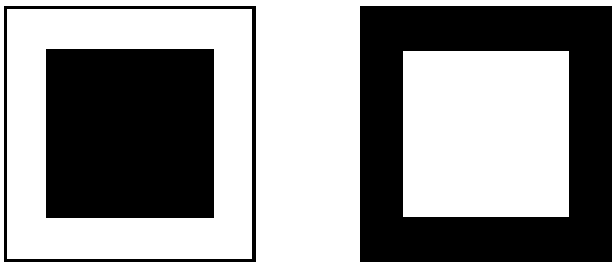

FIG. 6: Depicting two box patterns of fluid (black) and solid (white). On the left, the heat-generating phase is nonpercolating. On the right, it is percolating.

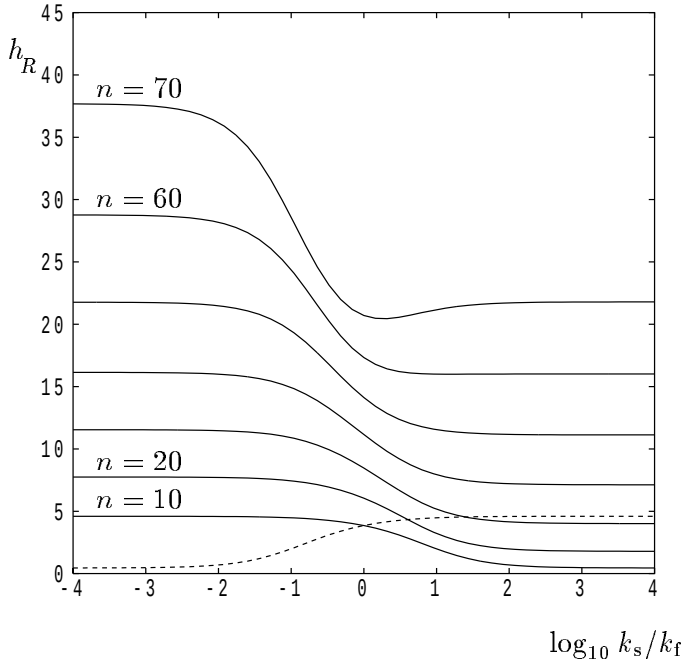

FIG. 7: Variation of h_R with $\log_{10} k_s/k_f$ on an 80×80 grid for heat-generating boxes of size $n \times n$, where $n = 10, 20, \cdots 70$. The dotted line corresponds to a 10×10 box of non-heat-generating material.

When expressed in terms of porosity, this becomes

$$h_R \simeq 28.5\epsilon \tag{53}$$

where $\epsilon = (n/N)^2$. The numerical value given in Eq. (53) is approximately the same as that given in Eq. (51), and this suggests that they may be related. Indeed, as the conductivity of the solid phase is extremely large, the temperature field of the solid phase is essentially uniform, and given that Eqs. (50) have unique solutions up to an arbitrary constant, we may set that constant to be such that $\hat{\theta}_s = 0$. Therefore we obtain a Poisson's equation for the solution within the fluid phase, where the boundary conditions are essentially uniform and set to zero. This argument is confirmed in Fig. 8, where isotherms are shown for a 40×40 heat-generating square within an 80×80 square. In the left-hand frames in that figure, we see that isotherms tend to become more concentrated within the fluid phase as $k_s/k_f \to \infty$, eventually reaching a state that is equivalent to the solution of Poisson's equation in a square since the temperature in the solid phase is uniform. Therefore we obtain $h_R = 28.4542\epsilon$.

It is possible to determine a similar formula for shapes other than squares. Perhaps of most interest is where the

fluid phase occupies a periodic array of circles. This is equivalent to the left-hand schematic in Fig. 6, where the central black square has been replaced by a circle. Details of the analysis may be found in the appendix, and we obtain the expression

$$h_{_R} = 8\pi\epsilon \simeq 25.1417\epsilon \tag{54}$$

This formula holds for all chosen porosities in the large $k_{\rm s}/k_{\rm f}$ limit.

When $k_{\rm s} \ll k_f$, the value of $h_{_R}$ does not obey a simple law like Eq. (54). This is because the main variation in the temperature field now lies within the solid phase, as shown in Fig. 8, and the detailed solution depends strongly on the porosity since the shape of the domain occupied by the solid phase changes with ϵ. However, it is possible to obtain an analytical form for $h_{_R}$ in the limit as $\epsilon \to 1$ because then the solution is dominated by the thermal fields in the four narrow channels along the periphery of the square. This analysis is rendered easier by appealing to the symmetry

$$h_{_R}{}^{\rm left}(k_{\rm s}/k_{\rm f}, \epsilon) = h_{_R}{}^{\rm right}(k_{\rm f}/k_{\rm s}, 1-\epsilon) \tag{55}$$

where "left" and "right" refer to the two box configurations shown in Fig. 6. In practice, this means that the right-hand column of Fig. 8 may be viewed either as $k_{\rm f} > k_{\rm s}$, where the fluid occupies the central square region, or as $k_{\rm s} > k_{\rm f}$, where the solid occupies the central square region. We shall adopt the latter viewpoint, and therefore we are considering the limit $\epsilon \to 0$. The analysis contained in the appendix yields the value

$$h_{_R} = 96 \tag{56}$$

for this configuration, which is equivalent to having very narrow fluid channels within a regular grid of square blocks.

5.4 Random Media

Most porous media, however, comprise either random networks of pores or random packings of particles. While all of the above configurations are of interest because they provide examples of precise results against which more realistic configurations may be compared, it is nevertheless essential to find out how random packings alter our idealized results. In the present section, we shall consider randomly assigned square grids with predetermined porosities, such as those shown in Fig. 9, and determine the value for $h_{_R}$ for each of them. We note that solutions remain independent of the diffusivity ratio, α, because of the analysis described in Section 4.2, and therefore our computations have used $\alpha = 1$.

Figure 10 gives some indicative results for $\log_{10}(h_{_R})$ for the following ranges of values: $N = 10$, 20, 40, and 80, $10^{-4} \le k_{\rm s}/k_{\rm f} \le 10^4$, and $\epsilon = 0.1, 0.2, \cdots 0.9$. Although we used only 100 random cases for each parameter set, the total number of configurations corresponding to all the possible arrangements of subcells far exceeds this number for all but the very smallest number of subsquares. For example, with $N = 10$ and $\epsilon = 0.1$, there are $100!/90!\,10! = 1.731 \times 10^{13}$ different configurations. Likewise, for $N = 10$ and $\epsilon = 0.5$, there are 1.0×10^{29} combinations, and for the worst case we consider, namely, for $N = 80$ and $\epsilon = 0.5$, there are 3.9×10^{1924} combinations. In all cases, our earlier striped and box configurations also represent possible configurations. We also note that the symmetry relation given by Eq. (55) is still obeyed for random configurations, and this means that curves for $\epsilon = 0.9$ are the mirror image about $k_{\rm s}/k_{\rm f} = 1$ of those for $\epsilon = 0.1$ on average. Observations may now be made based on the detailed behaviour of the curves.

First, it is clear that the finer the detail of the porous structure (i.e., the larger the value of N), the larger is the value of $h_{_R}$. This is true for all porosities and reflects the fact that conduction spreads more rapidly to neighboring cells when the cells are small, thereby enhancing LTE. It is also true that there is a decreasing amount of spread in the computed values of $h_{_R}$ as N increases. This result is of interest because the standard deviation of the one-dimensional random configurations behaves differently as N becomes large; we presume that this is due to the different connectivities between one and two dimensions.

At low porosities, as represented by $\epsilon = 0.1$, the solid phase dominates. In these cases, Fig. 9 shows that there is almost no spread in the distribution of $h_{_R}$ when the solid phase is highly conducting. Thus any temperature rise in the fluid is transmitted rapidly to the solid phase. Given such a low porosity, the great majority of the fluid cells are in isolation, and the heat is lost via all four boundaries of the cell. The clumping of cells is extremely rare at such porosities, but whenever clumping occurs, the transfer of heat is affected strongly, and $h_{_R}$ is reduced. This has already been seen for the striped configuration where $h_{_R} = 12$ and for the boxed configuration where Eq. (53), with $\epsilon = 0.1$, yields $h_{_R} = 4.45$. These latter two values are substantially lower than those represented in the $\epsilon = 0.1$ frames in Fig. 10 and represent the strong effect of structure, particularly contiguity of the heat-generating

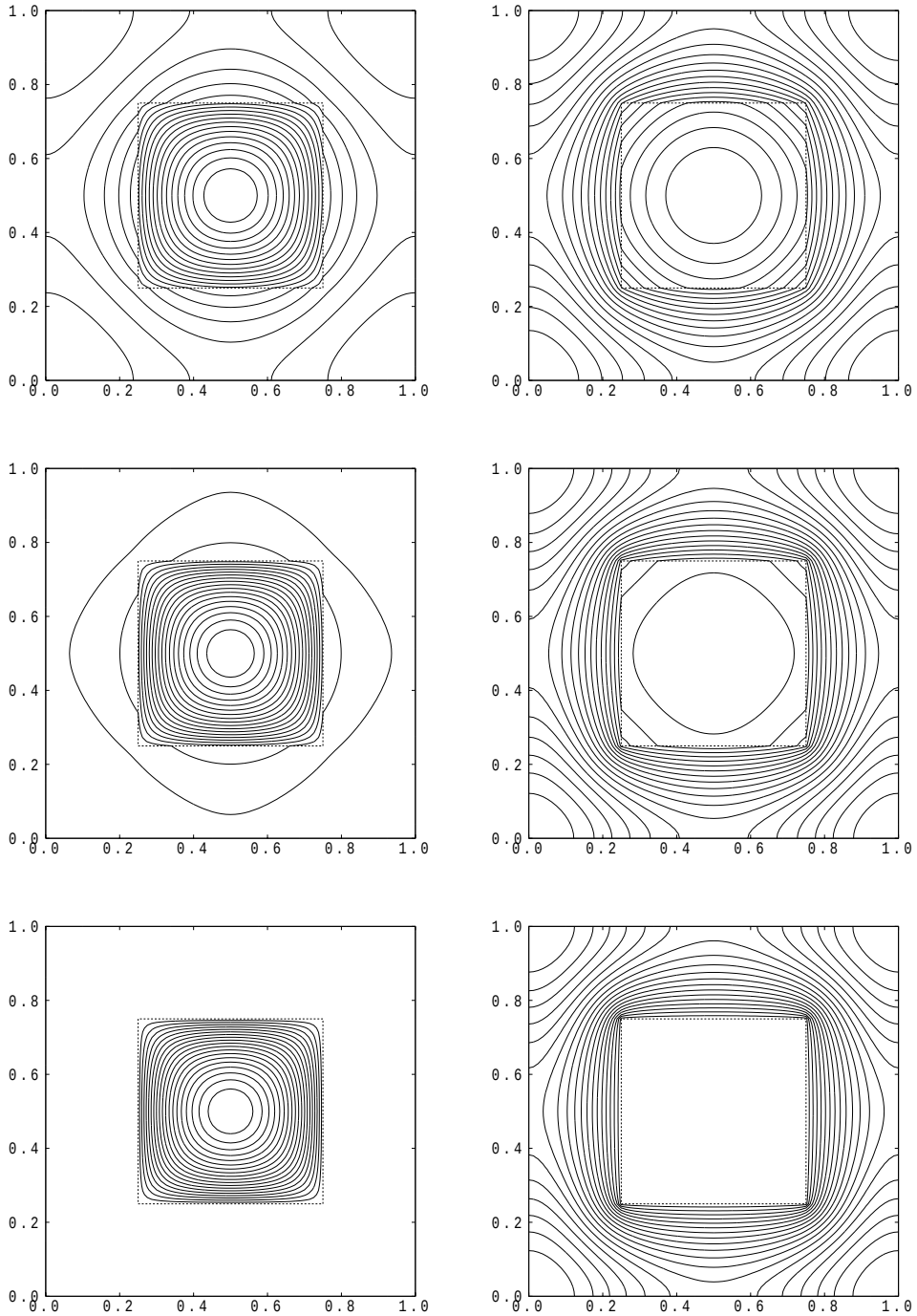

FIG. 8: Showing isotherms for the box configuration for $k_{\rm s}/k_{\rm f} = 3$, 10, and 100 in the upper, middle, and lower rows, respectively. The left-hand column corresponds to the fluid (heat-generating) phase occupying the central square, while the right column has the solid phase occupying the central square. The dotted line denotes the interface. Note that the right column also applies to the cases $k_{\rm s}/k_{\rm f} = 1/3$, 0.1, and 0.01 in the upper, middle, and lower rows, respectively, where the fluid phase occupies the central square.

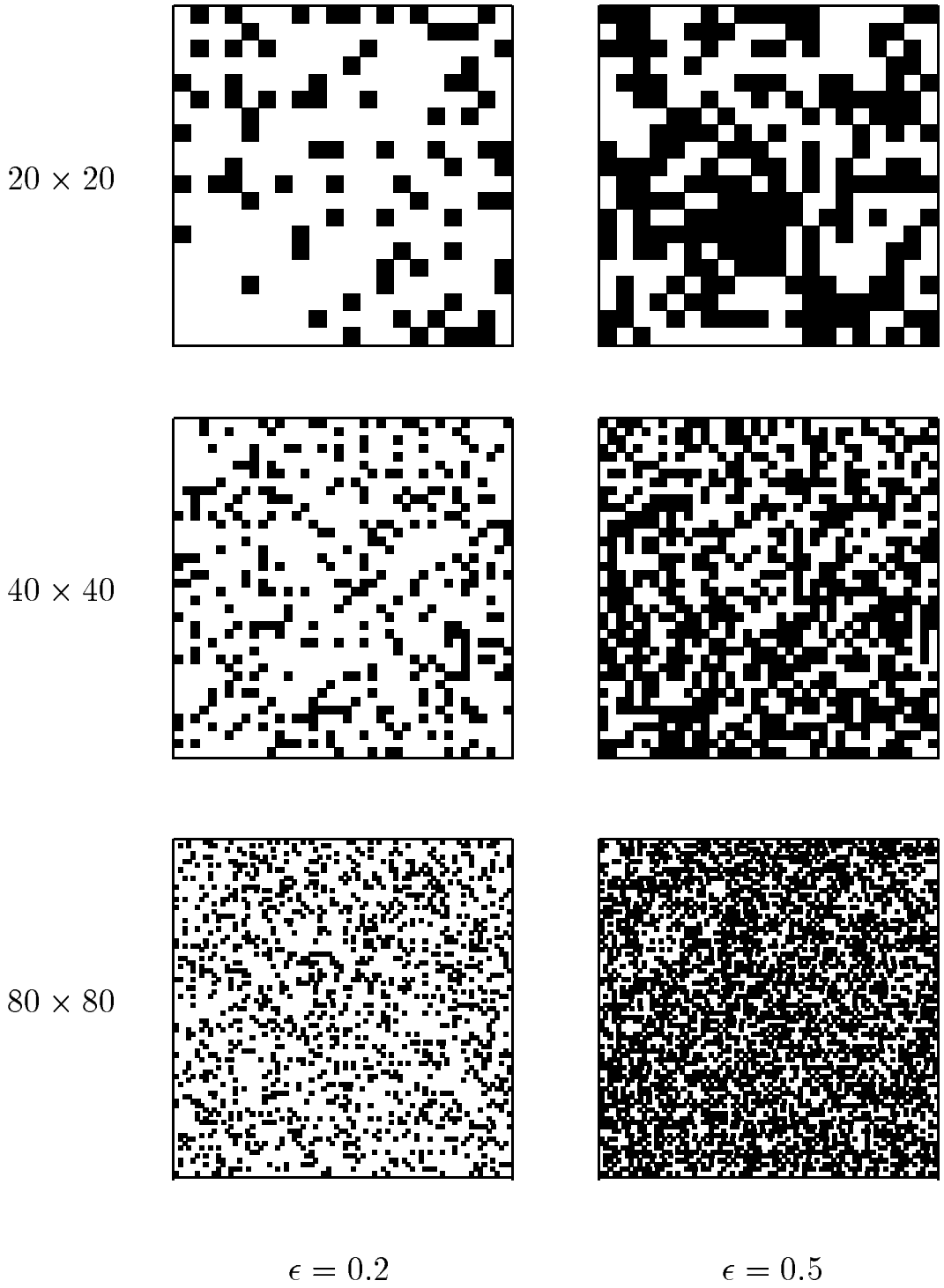

FIG. 9: Examples of two-dimensional boxes with random structure. Black indicates the heat-generating fluid cells, while white denotes the solid cells.

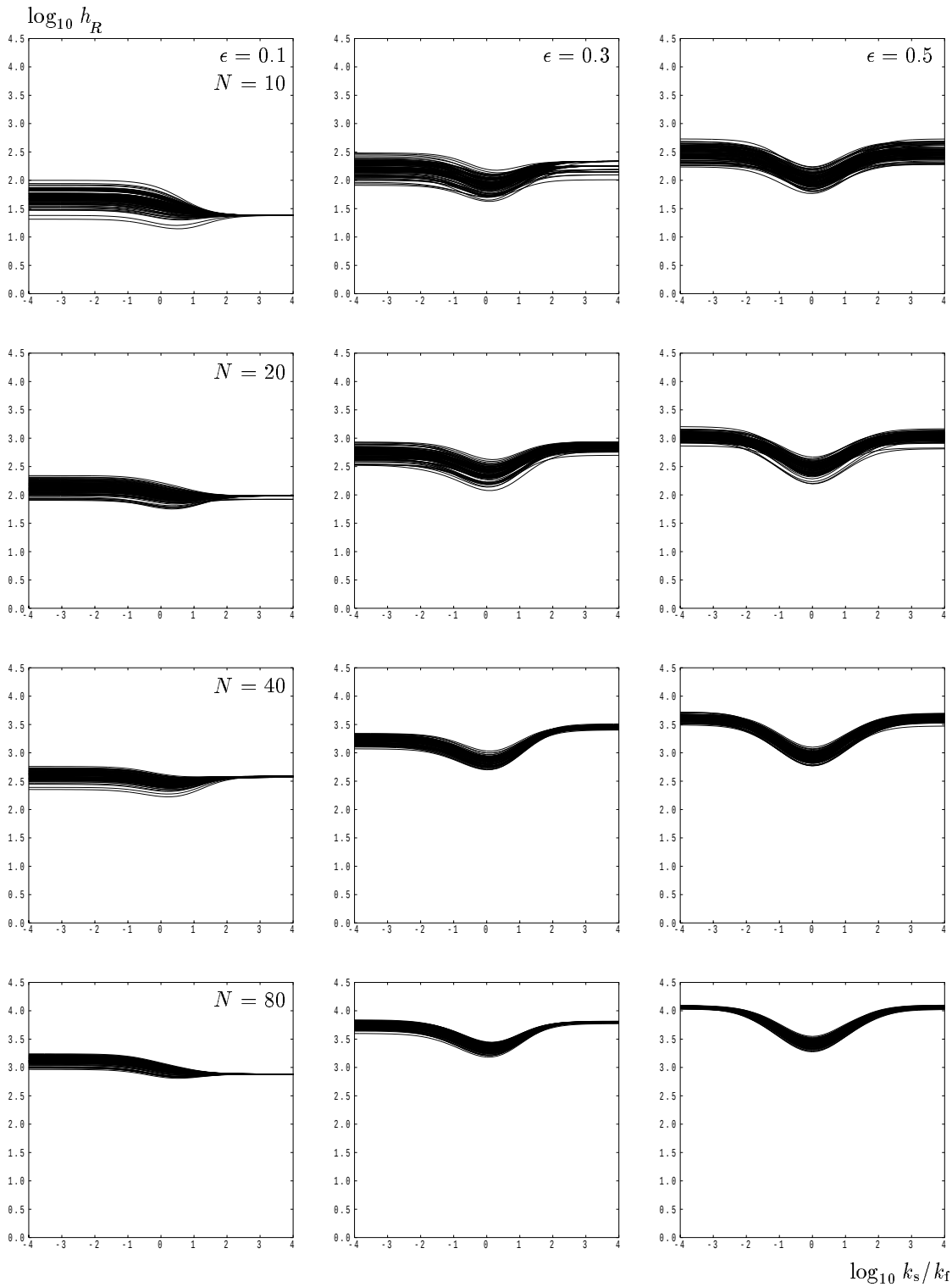

FIG. 10: The variation of h_R with conductivity ratio for 100 random $N \times N$ configurations with $N = 10$, 20, 40, and 80, and with the porosities $\epsilon = 0.1$, 0.3, and 0.5

phase, on the value of h_R. One example of this may be seen in the $N = 20$ case in Fig. 10.

Conversely, when the solid phase is a poor conductor relative to the fluid phase, there is a strong spread in the values of h_R. The highest values correspond to those configurations where the fluid cells are isolated. Whenever two or more neighbor one another, then a relatively large temperature rise occurs in the fluid, which further enhances LTNE and reduces the value of h_R.

As the porosity rises from 0.1 to 0.5, the value of h_R rises. When $N = 80$, this rise is a factor of approximately 10 whenever the conductivity ratio is very high or very low. At intermediate values of the conductivity ratio, that is, when the ratio is close to unity, then the rise is much less.

One aspect of the data displayed in Fig. 10 is shown in Fig. 11, where the variation of the mean value of h_R is presented. When $\phi = 0.1$, the variation of $\bar{h}_R$ with the conductivity ratio is not large, even when the logarithmic scale is taken into account, and especially so for large numbers of cells. Indeed, when $N = 80$, we may take $\bar{h}_R \sim 10^{3.1}$ to a fairly high degree of accuracy. However, the situation reverses as the porosity increases toward 0.5 when the total amount of variation in $\bar{h}_R$ becomes larger as N increases.

The necessary use of only 100 data sets for each combination of N, ϕ, and conductivity ratio means that the estimates of the standard deviation of h_R are likely to be highly inaccurate; this is certainly true for the one-dimensional cases presented earlier. However, Fig. 10 does give some indication of how the spread in the data changes with variations in each of the parameters.

5.5 Sierpinski Carpet

Finally, we consider an alternative, highly structured, but finely detailed configuration, the Sierpinski carpet. For the present purposes, we consider the fourth iteration, which may be represented using an 81×81 grid of cells. The numerical codes described earlier may also be used for this case since they were written in a very general form, requiring only a data file containing the pattern of conductivities to be input on execution.

The porosity of the Sierpinski carpet, as displayed in Fig. 12, is

$$\phi = 1 - \left(\frac{8}{9}\right)^4 = 0.3757 \tag{57}$$

and our results may be compared with those for stripes with precisely the same porosity, and with both the

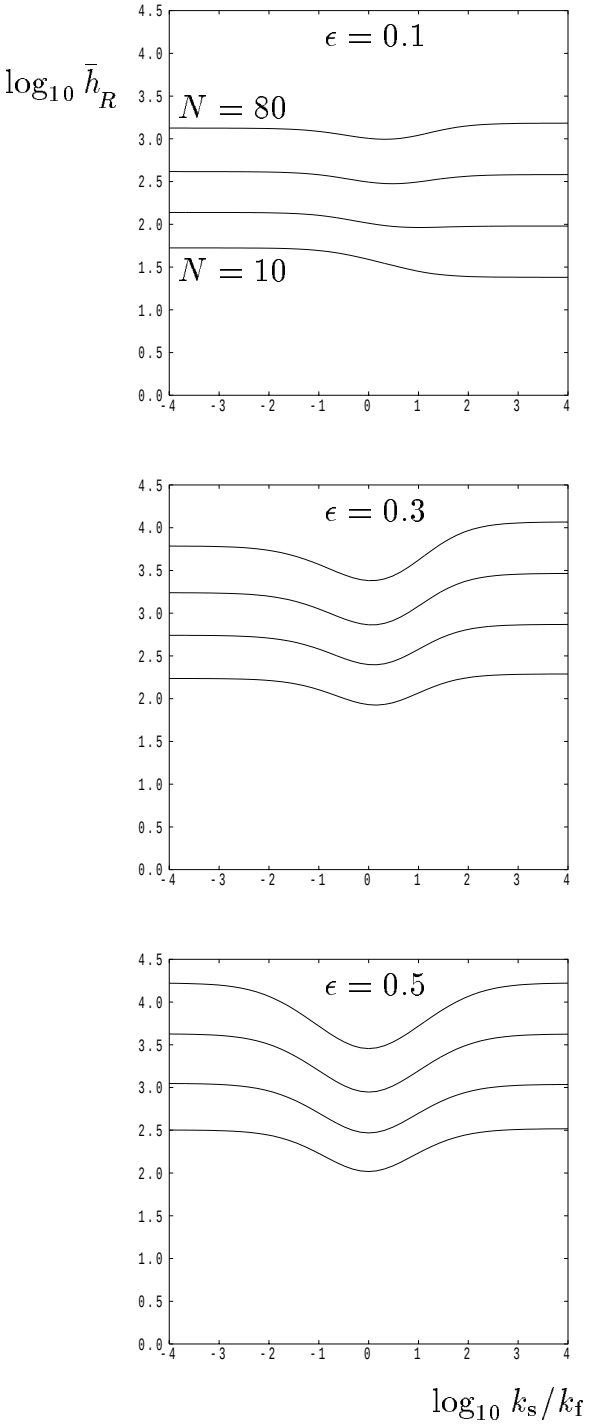

FIG. 11: The variation of the mean value of h_R with conductivity ratio for $\epsilon = 0.1$, 0.3, and 0.5, for $N = 10$, 20, 40, and 80

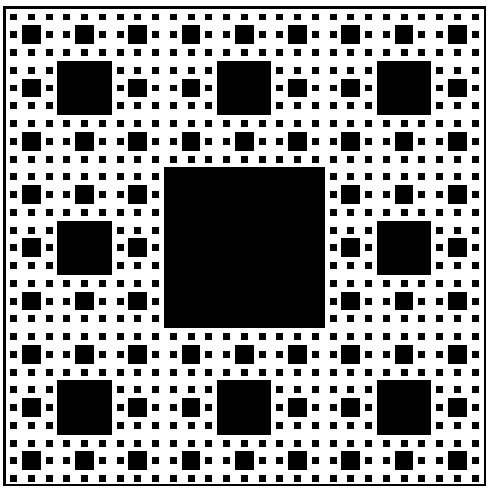

FIG. 12: Displaying the fourth iteration of the Sierpinski carpet

box and random configurations with precisely 49^2 heat-generating cells in a 80×80 square, since the porosity for this case is almost the same:

$$\epsilon = \left(\frac{49}{80}\right)^2 = 0.3752 \tag{58}$$

The detailed curve for $h_{_R}$ is shown in Fig. 13, together with those for all the other configurations mentioned. The overall magnitude of $h_{_R}$ lies between that for the box configuration, which is highly structured but is essentially one large cluster of the heat-generating phase, and that for the random configuration, which is highly unstructured and, given the porosity, is likely to contain many small clusters. The Sierpinski carpet contains both large clusters and isolated elements, and therefore it is not surprising that its value of $h_{_R}$ lies between these two cases.

6. CONCLUSIONS

In this article, we have resorted to solving the microscopic equations for unsteady conduction in a composite medium where one of the two phases generates heat at a uniform rate. The overall aim has been to gain some qualitative and quantitative understanding of how the value of h, the inter phase heat transfer coefficient, depends on the geometry of the porous medium and on its thermal prop-

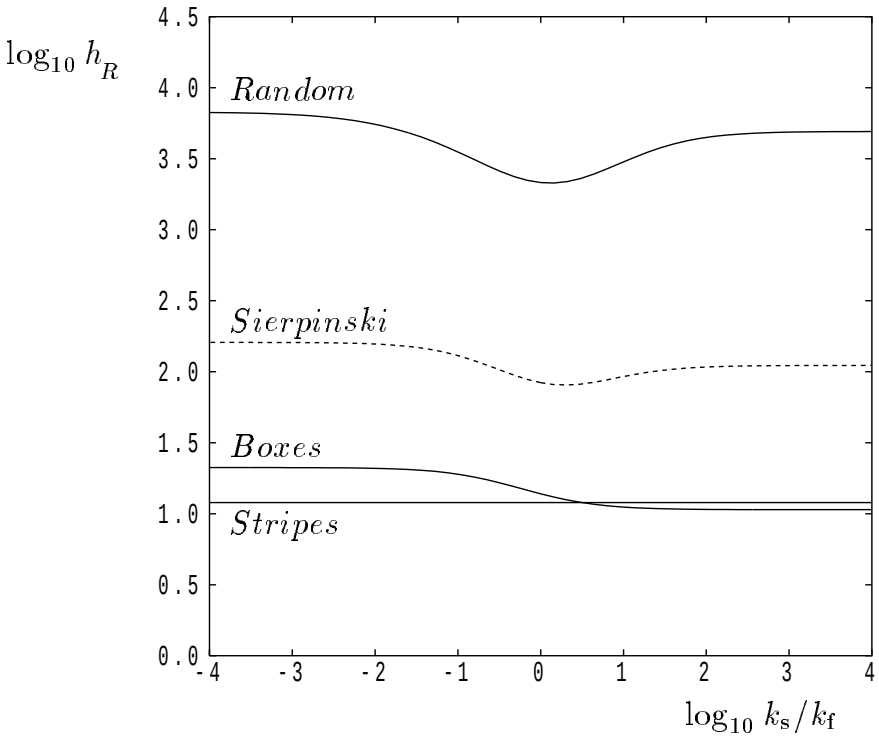

FIG. 13: Comparing the variation of $h_{_R}$ with conductivity ratio for stripes, boxes, random configurations, and the Sierpinski carpet. The porosity is approximately 0.375.

erties. This has been achieved by a direct comparison between the microscopic solutions and the simple analytical solution of the corresponding macroscopic system in which H, the nondimensional form of h, appears.

An analytical expression was obtained for striped domains, and highly accurate numerical solutions were found for the checkerboard pattern and its three-dimensional analogue. For these cases, the value of h_R is constant, and therefore we propose that this nondimensional quantity should be adopted as a suitable parameter to characterize the LTNE properties of the porous medium.

For boxes, the value of h_R ceases to be constant but nevertheless remains of $O(1)$ magnitude over all possible values of the conductivity ratio. There are some circumstances in which h_R varies very little with conductivity ratio (viz. for low values of the porosity). We have also determined analytical expressions for h_R for circular pores in a low-porosity medium when $k_s/k_s \gg 1$ (with an indication of how to obtain h_R for other shapes of pore) and for a square network of very narrow channels.

For random configurations, 100 cases for each parameter set were taken to gain some understanding of the range of variation of h_R and what its likely mean value is. Mean values for h_R and an indication of the spread of these values have also been given.

We have found that symmetry, as shown in Eq. (55), plays a central role in the absence of flow, a fact that has not been found in previous studies. However, it is highly unlikely that this symmetry persists in the presence of flow.

The present work forms an initial study into the computation of h, and we intend to make further progress by (1) considering other types of two-dimensional domain, (2) extending the analysis to three dimensions, (3) modeling of constant heat flux boundary conditions, and (4) considering the effect of fluid flow. Of these extensions, numbers 2 and 3 are currently in progress, while for 4, it will be essential to obtain data that reduce to those presented here as the Reynolds number decreases toward zero.

ACKNOWLEDGMENTS

This article was completed while the author was on study leave at the University of Bristol; he would like to thank his hosts for use of their facilities and their hospitality. The author would also like to thank Ivan Graham, University of Bath, for inviting him to give a talk at the workshop "Computation of Flow and Transport in Heterogeneous Media" in June 2006; this provided the initial impetus to begin work on the present topic. He would also like to thank the referees for useful comments.

REFERENCES

Anzelius, A., Über Erwärmung vermittels durchströmender Medien, *Zeit. Math. Mech.*, vol. **6**, pp. 291–294, 1926.

Carbonell, R. G. and Whitaker, S., Heat and mass transfer in porous media. In: *Fundamentals of Transport Phenomena in porous media*, Bear, J. and Corapcioglu, M. Y., (eds), Martinus Nijhoff, Dordrecht, 1984.

Dixon, A. G. and Cresswell, D. L., Theoretical prediction of effective heat transfer parameters in packed beds, *A. I. Chem. E. J.*, vol. **25**, pp. 663–676, 1979.

Dullien, F. A. L. *Porous Media Fluid Transport and Pore Structure*, Academic Press, New York, 1979.

Hsu, C. T. A closure model for transient heat conduction in porous media, *Trans. ASME J. Heat Transfer*, vol. **121**, pp. 733–739, 1999.

Hwang, G. J., Wu, C. C., and Chao, C. H., Investigation of non-Darcian forced convection in an asymmetrically heated sintered porous channel, *Trans. ASME J. Heat Transfer*, vol. **117**, pp. 725–732, 1995.

Khadrawi, A. F., Tahat, M. S., and Al-Nimr, M. A., Validation of the thermal equilibrium assumption in periodic natural convection in porous domains, *Int. J. Thermophys.*, vol. **26**, pp. 1633–1649, 2005.

Kuwahara, F., Shirota, M., and Nakayama, A., A numerical study of interfacial convective heat transfer coefficient in two-energy model for convection in porous media, *Int. J. Heat Mass Transfer*, vol. **44**, pp. 1153–1159, 2001.

Lee, D.-Y. and Vafai, K., Analytical characterization and conceptual assessment of solid and fluid temperature differentials in porous media, *Int. J. Heat Mass Transfer*, vol. **42**, pp. 423–435, 1999.

Ljung, A.-L., Lundström, S., and Tano, K., Heat, mass and momentum transfer within an iron ore pellet during drying, paper presented at the International Symposium on Advances in Computational Heat Transfer (CHT-08), Marrakech, Morocco, May 11–16 2008.

Luo, X., Guan, X., Li, M. L., and Roetzel, W., Dynamic behaviour of one-dimensional flow multistream heat exchangers and their networks, *Int. J. Heat Mass Transfer*, vol. **46**, pp. 705–715, 2003.

Nield, D. A. and Bejan, A., *Convection in Porous Media*, (3rd ed.), Springer, New York, 2006.

Quintard, M., Modelling local non-equilibrium heat transfer in porous media, *Proc. 11th Int. Heat Transfer Conf.*, vol. **1**, pp. 279–285, 1998.

Quintard, M., Kaviany, M., and Whitaker, S., Two-medium treatment of heat transfer in porous media: Numerical results for effective properties, *Adv. Water Resour.*, vol. **20**, pp. 77–94, 1997.

Quintard, M. and Whitaker, S., Theoretical analysis of transport in porous media. In: *Handbook of porous media*, Vafai K., (ed), pp. 1–51, Marcel Dekker, New York, 2000.

Rees, D. A. S., Vertical free convective boundary-layer flow in a porous medium using a thermal nonequilibrium model:

Elliptical effects, *J. Appl. Math. Phys.*, vol. **54**, pp. 437–448, 2003.

Rees, D. A. S., Bassom, A. P., and Siddheshwar, P. G., Local thermal non-equilibrium effects arising from the injection of a hot fluid into a porous medium, *J. Fluid Mech.*, vol. **594**, pp. 379–398, 2008.

Rees, D. A. S. and Pop, I., Vertical free convective boundary–layer flow in a porous medium using a thermal nonequilibrium model, *J. Porous Media*, vol. **3**, pp. 31–44, 2000.

Rees, D. A. S. and Pop, I., Local thermal nonequilibrium in porous medium convection, In: *Transport Phenomena in Porous Media III*, Ingham, D. B. and Pop, I., (eds.), Pergamon, New York, pp. 147–173, 2005.

Schumann, T. E. W. Heat transfer; a liquid flowing through a porous prism, *J. Franklin Institute*, vol. **208**, pp. 405–416, 1929.

Wakao, N. and Kaguei, S., *Heat and Mass Transfer in Packed Beds*, Gordon and Breach, New York, 1982.

Vadasz, P., Explicit conditions for local thermal equilibrium in porous media heat conduction, *Transp. Porous Media*, vol. **59**, pp. 341–355, 2005.

Whitaker, S., *The Method of Volume Averaging*, vol. **13** of *Theory and Applications of Transport in Porous Media*, Bear, J., (series ed), Kluwer, Dordrecht, 1999.

APPENDIX: SOME ASYMPTOTIC SOLUTIONS

In this appendix, we shall provide outline proofs of the expressions for $h_{_R}$ given in Eqs. (54) and (56), corresponding to the large–$k_{\rm s}/k_{\rm s}$ limit for circular pores and for small–ϵ channels, respectively.

For fixed values of ϵ, when $k_{\rm s}/k_{\rm s}$ becomes asymptotically large, the value of γ becomes asymptotically small. Therefore Eq. (50) reduces to the form

$$\nabla^2\hat{\theta}_{\rm f} + 1 = 0, \qquad \nabla^2\hat{\theta}_{\rm s} = 0 \tag{A1}$$

The interface conditions given in Eq. (22) also imply that the derivative of $\hat{\theta}_{\rm s}$ is zero on the interface, which means, in turn, that the solid phase has a uniform temperature, which we may set to be zero. Therefore the fluid phase has the boundary condition $\hat{\theta}_{\rm f} = 0$ on the interface.

For the first of the two configurations, we shall assume that the fluid phase is contained within a circle of radius R. Clearly $\hat{\theta}_{\rm f}$ will be axisymmetric, and therefore it satisfies the equation

$$r\hat{\theta}_{\rm f}'' + \hat{\theta}_{\rm f}' = -r \tag{A2}$$

where r is the radial coordinate and primes denote derivatives with respect to r. The solution is

$$\hat{\theta}_{\rm f} = (R^2 - r^2)/4 \tag{A3}$$

from which we may find the intrinsic temperature

$$\bar{\theta}_{\rm f} = \frac{1}{\pi R^2}\int_0^{2\pi}\int_0^R \frac{R^2 - r^2}{4}\, 2\pi r\, dr = \frac{R^2}{8} \tag{A4}$$

Equation (39) yields $H = 1/\bar{\theta}_{\rm f}$, while application of (16) yields an expression for h. These, together with Eq. (40), which is subject to $k_{\rm s} \gg k_{\rm f}$, yield the general formula for $h_{_R}$ under large $k_{\rm s}/k_{\rm f}$ conditions:

$$h_{_R} = \frac{\epsilon^2}{\bar{\theta}_{\rm f}} \tag{A5}$$

Given that we are dealing with a circle of radius R placed within a unit square, it is clear that $\epsilon = \pi R^2$. Hence Eq. (A5) yields the required result,

$$h_{_R} = 8\pi\epsilon \tag{A6}$$

This type of analysis may be extended to any pore shape. All that is required is a numerical or analytical solution of the Poisson's Eq. (A1a), followed by a determination of the mean value of the resulting temperature field. The porosity is a function of the linear dimension of the pore, and therefore $h_{_R}$ may be found for that domain.

The second configuration is an example of this process. Here the fluid is contained within narrow channels, which separate equally spaced solid blocks, such as is illustrated in the right-hand part of Fig. 5(b). We shall choose to use δ as the width of the fluid regions, as shown in that figure, which, due to the periodic nature of the domain, means that the channels are of width 2δ, and therefore the boundaries of the domain require a zero derivative boundary condition. When δ is very small, we may neglect the corner regions, and therefore the temperature within the lower channel is given by

$$\hat{\theta}_{\rm f} = \frac{\delta^2 - y^2}{2} \tag{A7}$$

The mean temperature within this channel is easily found to be $\bar{\theta}_{\rm f} = \delta^2/3$, which is the same as for the other three channels. The value of δ is related to the porosity by $\epsilon = 4\delta$ to leading order, and therefore we find that $\bar{\theta}_{\rm f} = \epsilon^2/48$. On using Eq. (A5) we obtain the previously quoted result,

$$h_{_R} = 48 \tag{A8}$$

Finally, for this configuration, it is important to note that while the separate limits $k_{\rm s}/k_{\rm f} \to \infty$ and $\epsilon \to 0$ both contribute to $\gamma \to 0$, the two limiting processes must be such that $\epsilon/k_{\rm f}$ remains much greater than $(1-\epsilon)/k_{\rm s}$ in the definition of $h_{_R}$ in Eq. (40).